ACS NANO

www.acsnano.org

ARTICLE

Predicting Gas Separation through Graphene Nanopore Ensembles with Realistic Pore Size Distributions

Zhe Yuan, Ananth Govind Rajan, Guangwei He, Rahul Prasanna Misra, Michael S. Strano, and Daniel Blankschtein*

Cite This: *ACS Nano* 2021, 15, 1727−1740

Read Online

ACCESS | Metrics & More | Article Recommendations | Supporting Information

ABSTRACT: The development of nanoporous single-layer graphene membranes for gas separation has prompted increasing theoretical investigations of gas transport through graphene nanopores. However, computer simulations and theories that predict gas permeances through individual graphene nanopores are not suitable to describe experimental results, because a realistic graphene membrane contains a large number of nanopores of diverse sizes and shapes. With this need in mind, here, we generate nanopore ensembles *in silico* by etching carbon atoms away from pristine graphene with different etching times, using a kinetic Monte Carlo algorithm developed by our group for the isomer cataloging problem of graphene nanopores. The permeances of H_2, CO_2, and CH_4 through each nanopore in the ensembles are predicted using transition state theory based on classical all-atomistic force fields. Our findings show that the total gas permeance through a nanopore ensemble is dominated by a small fraction of large nanopores with low energy barriers of pore crossing. We also quantitatively predict the increase of the gas permeances and the decrease of the selectivities between the gases as functions of the etching time of graphene. Furthermore, by fitting the theoretically predicted selectivities to the experimental ones reported in the literature, we show that nanopores in graphene effectively expand as the temperature of permeation measurement increases. We propose that this nanopore "expansion" is due to the desorption of contaminants that partially clog the graphene nanopores. In general, our study highlights the effects of the pore size and shape distributions of a graphene nanopore ensemble on its gas separation properties and calls into attention the potential effect of pore-clogging contamination in experiments.

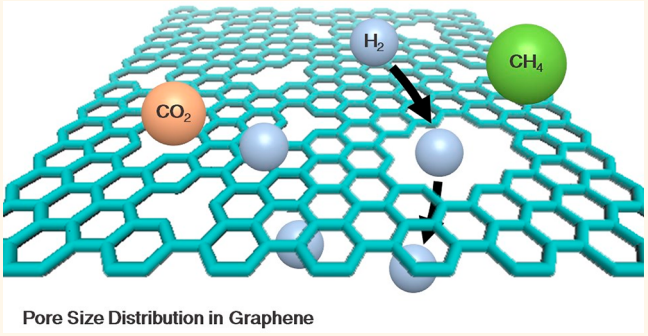

KEYWORDS: *graphene nanopore, nanopore isomers, nanopore ensembles, gas separation, pore size distribution, kinetic Monte Carlo simulation*

Nanoporous single-layer graphene shows high promise as a next-generation gas separation membrane, primarily due to its atomic thickness.[1−3] Compared to the pore matrices inside conventional polymer membranes, nanopores in single-layer graphene have negligible pore lengths. As a result, gas transport through graphene nanopores experiences minimal internal resistance and is instead dominated by the transport resistances at the pore entrance and the pore exit.[4] The minimal internal transport resistance across the pore makes nanoporous single-layer graphene potentially highly permeable to gases.[5] With an appropriate pore size distribution and a high areal pore density, a nanoporous single-layer graphene membrane can surpass the permeance−selectivity Robeson upper bound[6] for conventional polymer membranes,[7] thereby highlighting its potential for gas separation applications.[8,9]

The dominance of the entrance/exit transport resistances leads to a fundamentally different theoretical description of gas permeation through a graphene nanopore compared to that through a thick polymer membrane. The solution-diffusion model describes the permeation of gas molecules through

Received: November 10, 2020
Accepted: January 6, 2021
Published: January 13, 2021

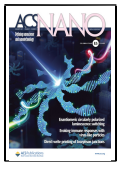

https://dx.doi.org/10.1021/acsnano.0c09420
ACS Nano 2021, 15, 1727−1740

polymer membranes, where the interior diffusive resistance is dominant.[10] In contrast, for graphene nanopores, our group showed that the total gas transport resistance can be decomposed into three components: the translocation resistance related to the cross-pore energy barrier, the direct impingement resistance, and the surface diffusion resistance.[4,11] Specifically, we demonstrated that the diameter of a graphene nanopore needs to be lower than 0.6 nm in order to achieve a moderate CO_2/CH_4 selectivity greater than 5.[4] Below this diameter threshold, gas permeation through graphene nanopores is governed by the translocation energy barrier, which can be predicted by the transition state theory, given an all-atom force field.[11] Using this theoretical framework, we showed that the gas separation performances of two individual graphene nanopores fabricated by Koenig *et al.*[12] are close to, albeit lower than, the permeance−selectivity upper bound that we predicted for graphene nanopores.[11]

Interestingly, as the relevant data sets transition from investigating individual nanopores to investigating a large number of nanopores in a membrane, and from measurements at room temperature to measurements at a series of temperatures, our theoretical predictions face challenges in matching every experimental observation. The first challenge is that there is not always a representative nanopore structure that yields a selectivity of a gas pair similar to that observed experimentally. For example, Huang *et al.* and Zhao *et al.* measured H_2/CH_4 selectivities ranging from 5 to 25 using single-layer graphene membranes containing millions to billions of nanopores.[7,13] However, our theory cannot assign every selectivity value to an individual nanopore structure, because nanopores are formed in specific shapes and sizes and their selectivities vary discretely, rather than in a continuous manner.[14] Another challenge is that our theory cannot reproduce the apparent energy barriers that are directly derived by fitting experimentally measured gas permeances at different temperatures to the Arrhenius equation. To be more precise, multiple studies conducted by our group[15] and others[7,13] have shown that almost all the experimental gas permeances increase as a function of temperature, which is indicative of positive apparent energy barriers based on the Arrhenius equation. Specifically, apparent energy barriers between 10 and 30 kJ mol^{-1} have been measured for He, H_2, CO_2, and CH_4, respectively, and their values appear invariant regardless of how the nanopores were created.[7,13,16] Unfortunately, our previous theoretical calculation results[11] cannot identify a nanopore that matches all the apparent energy barriers simultaneously, assuming that the nanopore structure does not change as a function of temperature.

The two challenges discussed above clearly indicate that it is not sufficient to approximate a large pore ensemble as a single pore. When created randomly in a graphene lattice by an etching method (the most common scalable way to create nanopores), the nanopores are distributed in terms of their sizes and shapes, instead of being identical.[14,17−19] Here, the nanopore size refers to the number of carbon atoms removed from the pristine graphene lattice. Due to the randomness of the etching events, when the pore diameter is within 1 nm, the pore size distribution is usually positively skewed (*i.e.*, the right tail is longer) and is typically fitted to a log-normal or Poisson distribution.[20,21] In addition, our group has previously shown that multiple nanopore isomers with different pore shapes may exist for the same pore size and that their relative populations can be predicted by a kinetic Monte Carlo (KMC) algorithm.[14] The predicted most-probable isomers match transmission electron microscopy (TEM) images of graphene nanopores with high consistency for each pore size, demonstrating the ability of the KMC algorithm to model the real pore etching kinetics encountered in the experiments.[14]

The pore size and pore shape distributions result in variations in the gas permeance through the nanopores in a nanopore ensemble. Accordingly, in this work, in order to predict the overall gas permeance through a nanopore ensemble, we propose to (i) simulate the pore size and shape distributions of nanopores generated by graphene etching, (ii) predict the gas permeance through each nanopore, (iii) add up the permeances, and (iv) compare the predicted total gas permeances and selectivities to those measured experimentally. In more detail, we generate a large number of graphene nanopore structures *in silico* using the KMC etching algorithm developed recently by our group.[14] The principal knob that is varied during nanopore generation in the simulations is the etching time t. The generated nanopores are then checked for uniqueness using a previously developed cataloging algorithm based on chemical graph theory.[14] Subsequently, the permeances of H_2, CO_2, and CH_4 through each unique nanopore at temperatures ranging from 30 to 150 °C are calculated according to the transition state theory.[11] We chose these three gases because their separations are crucial in commodity-scale chemical processes, such as synthetic gas and natural gas processing.[22,23] We then evaluated the effect of the etching time t and the temperature on the gas permeances and the selectivities of the generated nanopore ensembles. Finally, we attempted to fit the theoretical predictions to available experimental data sets and proposed that the graphene nanopores should be allowed to effectively expand at a higher temperature in order to better fit the experimental data. We also proposed a possible mechanism to explain the expansion of the nanopores with temperature.

RESULTS AND DISCUSSION

Theoretical Predictions. Consider a nanopore ensemble consisting of N nanopores (i = 1, 2, ..., N), with their respective gas permeances per pore K_i (*i.e.*, the pressure-normalized gas flow rate, unit: mol s^{-1} Pa^{-1}). The total gas permeance $K = \sum_{i=1}^{N} K_i$. Using the following set of equations (eqs 1−4) developed by our group,[4,11] we can predict the gas permeance per pore K_i through each nanopore i:

$$K_{\text{trans},i} = \frac{H_{\text{pore}}(T)}{L_i}\sqrt{\frac{k_B T}{2\pi m}}\exp\left(\frac{\Delta S_i^{\ddagger}}{k_B}\right)\exp\left(-\frac{\Delta E_i^{\ddagger}}{k_B T}\right) \quad (1)$$

$$K_{\text{direct},i} = \delta_i\sqrt{\frac{\pi}{2mk_B T}}\frac{D_{p,i}^2}{4} \quad (2)$$

$$K_{\text{surface},i} = \gamma_i\sqrt{\frac{\pi k_B T}{2m}}D_{p,i}H_{\text{surf}} \quad (3)$$

$$K_i = [K_{\text{trans},i}^{-1} + (K_{\text{direct},i} + K_{\text{surface},i})^{-1}]^{-1} \quad (4)$$

Equation 1 predicts the gas transport rate $K_{\text{trans},i}$ (normalized by the pressure difference) of translocation from the pore mouth on one side to that on the other side.[11] In eq 1, the energy barrier $\Delta E_i^{\ddagger}$ and the entropy barrier $-\Delta S_i^{\ddagger}$ through nanopore i are calculated by fitting the Helmholtz free energy

https://dx.doi.org/10.1021/acsnano.0c09420
ACS Nano 2021, 15, 1727−1740

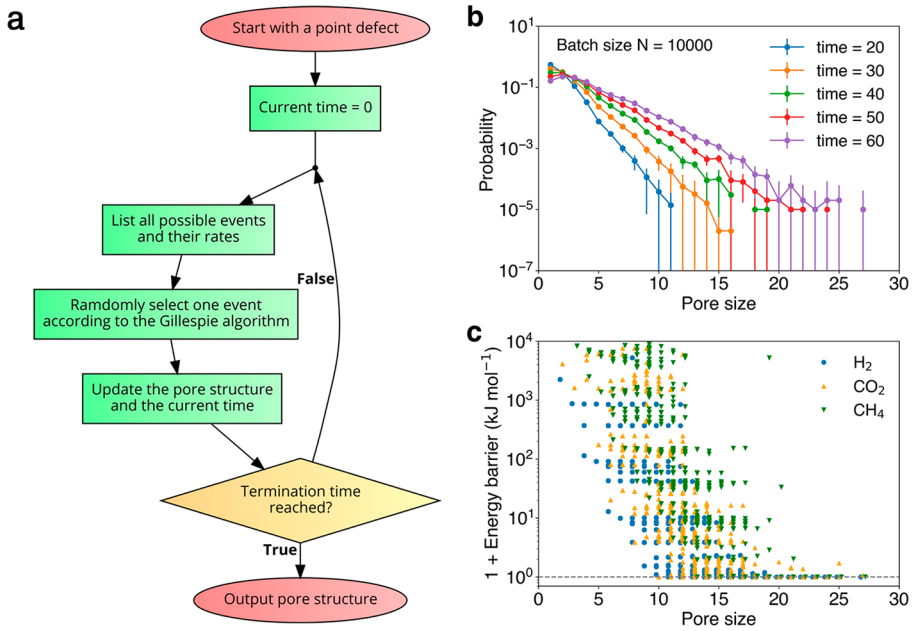

Figure 1. (a) Flowchart of the kinetic Monte Carlo algorithm used to generate graphene nanopore structures with a predefined etching time. (b) Simulated size distributions of nanopores generated at various etching times. Some confidence intervals extend to negative values and are not fully shown on the log-*y* axis. (c) Scatter plot of theoretically predicted energy barrier values of H_2, CO_2, and CH_4 as a function of pore size. Each pore size corresponds to multiple isomers and, hence, to multiple possible energy barriers. Scatter points are slightly shifted horizontally to prevent overlap. The horizontal black dashed line corresponds to a zero energy barrier.

barriers $\Delta A_i^{\ddagger} = \Delta E_i^{\ddagger} - T\Delta S_i^{\ddagger}$ to temperature T and then finding the intercepts and the slopes, respectively. The graphene−gas interactions are modeled at an all-atomistic level using Lennard-Jones potentials. For simplicity, in the calculations, the nanopores are assumed to be nonterminated. Additional details about the calculation of the Helmholtz free energy profile are provided in the Methods section. Furthermore, in eq 1, H_{pore} represents the average number of gas molecules adsorbed to the pore mouth per unit bulk pressure under adsorption equilibrium, and L_i is the full width at half-maximum of the partition function of the gas−pore system, $Q_i(z)$, as a function of the gas molecule's vertical distance to the graphene basal plane, z. Note that $Q_i(z) = \exp[-A_i(z)/k_BT]$, where $A_i(z)$ is the Helmholtz free energy profile associated with pore crossing for nanopore i (see Methods for additional details). Other parameters in eq 1 include k_B, the Boltzmann constant, and m, the molecular weight of the gas molecule. It is worth noting that the entropy barrier $-\Delta S_i^{\ddagger}$ is, in fact, a key contributor to the gas separation and should not be ignored (see Supporting Information (SI) Section S1 for more details).

Equation 2 predicts the direct impingement rate of gas molecules approaching the nanopore from the bulk, where $D_{p,i}$ is the equivalent pore diameter and δ_i is a correction factor accounting for the success rate of the direct impingement attempts (see Methods for additional details about $D_{p,i}$ and δ_i).[4] Equation 3 predicts the surface diffusion rate of gas molecules approaching the nanopore along the graphene surface, where H_{surf} is the areal density of gas molecules adsorbed on the "bulk" graphene surface (far away from the nanopore) per unit bulk pressure, and γ_i is a correction factor accounting for the success rate of the surface diffusion pathway (see Methods for additional details about γ_i).[4] The values of H_{pore} and H_{surf} can be calculated based on the Helmholtz free energy profile of gas molecules (see Methods). The gas permeance per pore K_i is then derived according to eq 4. In this work, $K_{trans,i}$ is typically much smaller than $K_{direct,i} + K_{surface,i}$, because the nanopores are sufficiently small and the energy and entropy barriers make the translocation step rate-determining ($K_i \approx K_{trans,i}$). Utilizing eqs 1−4, we predict the permeance per pore K_i through each nanopore in an ensemble for H_2, CO_2, and CH_4.

One important metric to characterize the temperature dependence of the total permeance of a nanopore ensemble K is the average energy barrier $\overline{\Delta E^{\ddagger}}$. Note that $\overline{\Delta E^{\ddagger}}$ is equal to the average of the energy barriers of all the nanopores weighted by their respective gas permeances (see SI Section S2 for the derivation); that is,

$$\overline{\Delta E^{\ddagger}(T)} = \frac{\sum_{i=1}^{N} K_i(T)\Delta E_i^{\ddagger}}{\sum_{i=1}^{N} K_i(T)} \quad (5)$$

Note that because the gas permeance through an individual nanopore K_i is temperature dependent, the average energy barrier $\overline{\Delta E^{\ddagger}}$ is strictly temperature dependent as well. However, when the pore sizes have a realistic distribution, $\overline{\Delta E^{\ddagger}}$ is dominated by low-energy-barrier nanopores because they weight significantly more in the sums in eq 5.

The formalism above for predicting the gas permeance applies for any pore size distributions. Next, we will discuss how a realistic nanopore ensemble is generated. Pore etching simulations *in silico* were carried out using a KMC algorithm (Figure 1(a); additional details are provided in the Methods section). Starting from a single point defect in pristine graphene, carbon atoms were removed sequentially, at rates that were estimated according to the energy barriers provided in ref 14. In this manner, graphene nanopore structures that match well with TEM images are generated.[14] Typically, because there are multiple choices regarding which carbon

https://dx.doi.org/10.1021/acsnano.0c09420
ACS Nano 2021, 15, 1727−1740

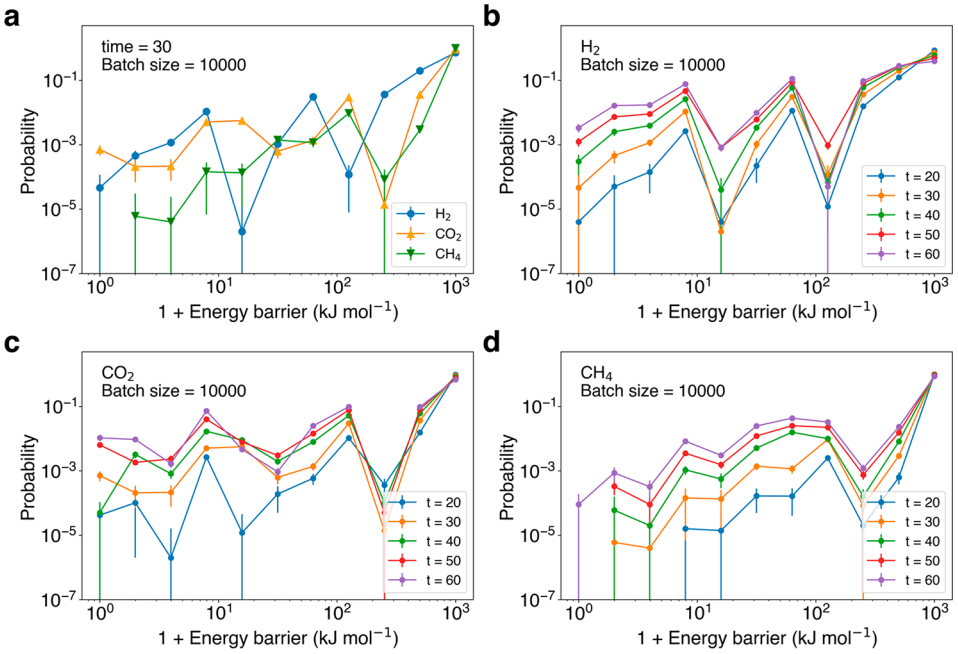

Figure 2. (a) Distribution of theoretically predicted energy barriers of pore crossing for H_2, CO_2, and CH_4 with etching time = 30. Distribution of energy barriers of pore crossing for (b) H_2, (c) CO_2, and (d) CH_4 with etching time from 20 to 60. Energy barriers greater than 10^3 kJ mol^{-1} are treated as 10^3 kJ mol^{-1}. Missing data points indicate zero nanopores in the corresponding bins.

atom to etch away at each step, we utilized the Gillespie algorithm to randomly select one of them.[24] Each possible carbon etching event j has a rate r_j, and the probability that event j is chosen is r_j/r_{tot}, where r_{tot} is the sum of all the r_j values. The expected value of the time interval $E(\Delta t)$ of this etching step is $1/r_{tot}$, and the time interval Δt is randomly sampled from an exponential distribution with a probability density function given by

$$P(\Delta t) = r_{tot} e^{-r_{tot}\Delta t} \quad (6)$$

As shown in Figure 1(a), the current (c) time t_c was updated after each etching event ($t_c \rightarrow t_c + \Delta t$). The iteration terminated when the current time t_c exceeded the predetermined etching time t. For each etching time t, the KMC algorithm was run repeatedly to generate 500 000 nanopores separated in 50 batches of size N = 10 000 each.

Figure 1(b) shows the simulated pore size distributions for etching times ranging from 20 to 60, with a batch size of 10 000. The error range represents the estimated standard deviation of the probabilities from the 50 batches. As the etching time increases, the pore size distribution shifts to the right, indicating an increase in the average pore size. Note that the etching time used here is dimensionless, because the etching rate r_j is nondimensionalized by the typical atomic vibrational frequency of 10^{13} Hz. In other words, when the prefactor of the carbon etching reaction is 10^{13} s^{-1}, the etching time t has a unit of second (see Methods). In order to achieve a considerable selectivity, the etching time cannot be too high. Otherwise, the largest nonselective nanopore will dominate the overall gas flux and make the entire nanopore ensemble nonselective. As a reference, pore size = 30 corresponds to a pore diameter of ∼1 nm for a circular nanopore. This criterion restricts relevant etching times to be below ∼100. In this etching time range, the probability distribution decays exponentially as the pore size increases (Figure 1(b)), and the majority of the nanopores are smaller than size 5. Further, the probability of generating larger nanopores is prone to high uncertainty, where the error range increases significantly as the pore size increases.

Although the larger nanopores are a minor species in the nanopore ensemble, they do not necessarily contribute a minority of the total gas permeance, because they present low energy barriers for gas permeation. Figure 1(c) shows that the simulated energy barriers of gases crossing the nanopores, $\Delta E^{\ddagger}$, decay rapidly by orders of magnitude as the pore size increases. Each pore size corresponds to multiple energy barrier values because of the existence of nanopore isomers (same size but different shapes). Some isomers with very high energy barriers have elongated shapes and are rarely generated in our KMC algorithm. Note that on the y axis of Figure 1(c) we added 1 to the energy barrier values (in kJ mol^{-1}) in order to prevent zero-energy-barrier nanopores from disappearing on the log scale used. Those zero-energy-barrier nanopores emerge as the pore size reaches ∼10, corresponding to a pore diameter of ∼0.6 nm if the pore is approximately circular.

The low fraction of large nanopores in a nanopore ensemble results in a low fraction of low-energy-barrier nanopores. Figure 2(a) plots the histograms of the theoretically predicted energy barriers of H_2, CO_2, and CH_4 crossing 10 000 nanopores generated by an etching time of 30. The fractions of nanopores with relatively low energy barriers, *e.g.*, $\Delta E^{\ddagger}$ < 10 kJ mol^{-1} (∼$4k_BT$ at room temperature) are 1.2%, 0.6%, and 0.015% for H_2, CO_2, and CH_4, respectively (Figure 2(a)). Modest change to this threshold does not affect the validity of our following findings. This ordering is consistent with the ranking of their kinetic diameters (H_2: 0.29 nm, CO_2: 0.33 nm, CH_4: 0.38 nm), because a smaller gas molecule is less impeded from crossing the nanopores. Due to the stochasticity during nanopore generation, the fraction of the low-energy-barrier nanopores has a high relative error, especially when the etching time is short (Figure 2(b)−(d)). Figure 2(b)−(d) also show that the fraction of low-energy-barrier nanopores generally

https://dx.doi.org/10.1021/acsnano.0c09420
ACS Nano 2021, 15, 1727−1740

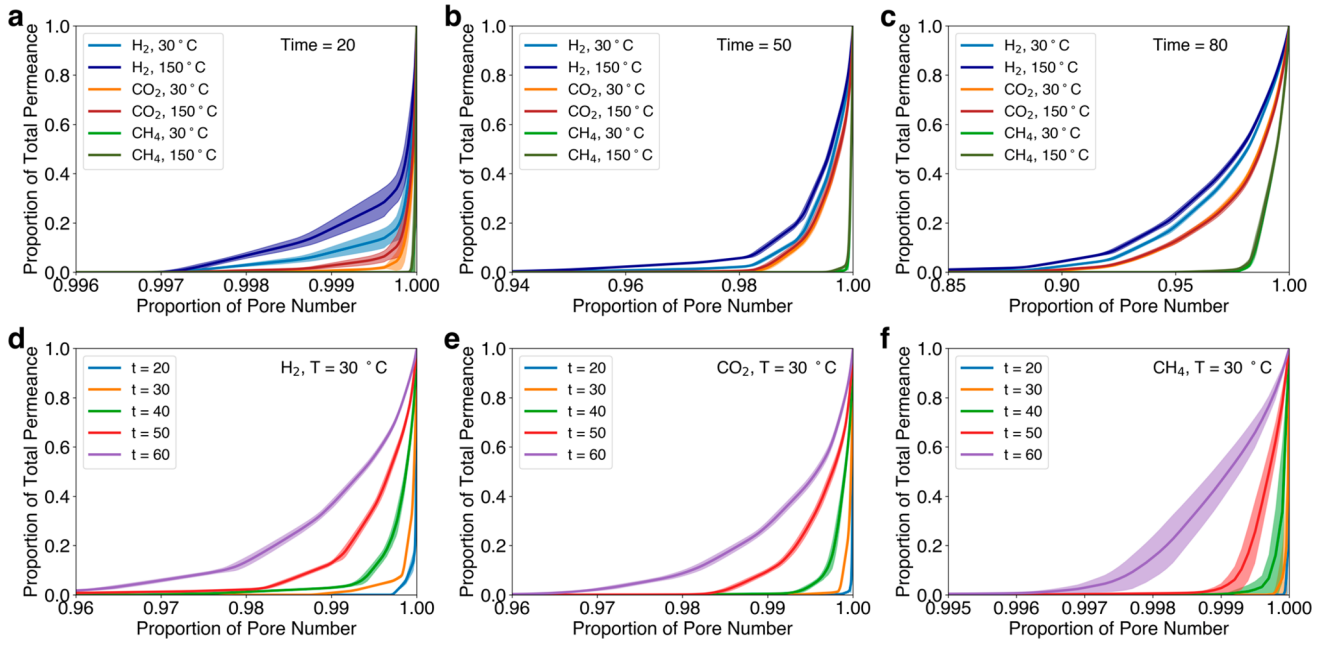

Figure 3. Lorenz curves of theoretically predicted H_2, CO_2, and CH_4 permeance distributions at 30 and 150 °C for nanopore ensembles generated with etching times of (a) 20, (b) 50, and (c) 80, respectively. Lorenz curves of theoretically predicted (d) H_2, (e) CO_2, and (f) CH_4 permeance distributions at 30 °C for nanopore ensembles generated with various etching times from 20 to 60.

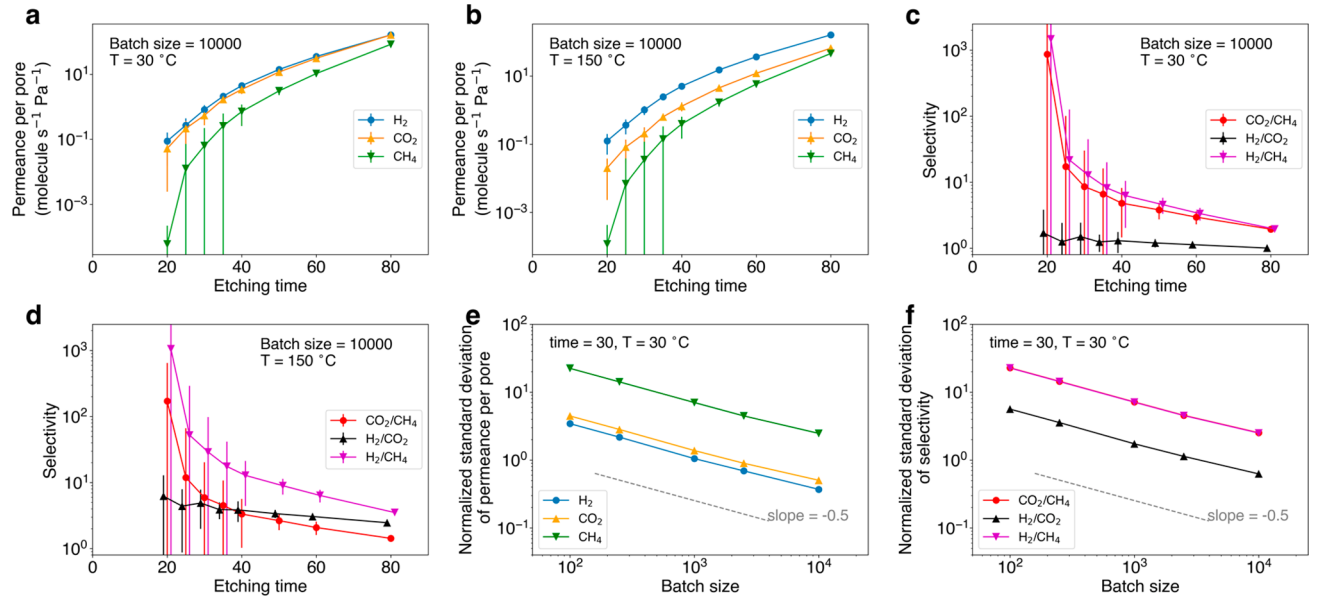

Figure 4. Theoretically predicted permeances per pore of H_2, CO_2, and CH_4 as functions of the etching time at (a) 30 °C and (b) 150 °C. Theoretically predicted selectivities of CO_2/CH_4, H_2/CO_2, and H_2/CH_4 as functions of the etching time at (c) 30 °C and (d) 150 °C. In (c) and (d), some data points are horizontally shifted to avoid overlap of their error bars. The normalized standard deviations (relative errors) of (e) the permeance per pore and (f) the selectivity both decrease as the batch size N increases.

increases as the etching time increases, in accordance with the pore size distribution shown in Figure 1(b).

For each nanopore ensemble generated with each etching time t, we predict the individual gas permeances K_i through every nanopore and the total permeance K using eqs 1−4. In order to evaluate the unevenness of the gas permeance distribution in a nanopore ensemble, we plot the Lorenz curves of the permeance distributions of H_2, CO_2, and CH_4 through different nanopore ensembles at two temperatures, 30 and 150 °C (Figure 3). The Lorenz curve was developed by Max O. Lorenz to represent income inequality.[25] It plots the percentiles of population on the x axis according to income, and the cumulative income on the y axis. Here, we borrow this concept and plot the percentiles of nanopores ordered from low to high gas permeance on the x axis and the proportion of their cumulative gas permeance on the y axis. Figure 3(a) shows the Lorenz curves of the theoretically predicted H_2, CO_2, and CH_4 permeance distributions through the nanopore ensemble generated with etching time t = 20 at 30 and 150 °C. As indicated by the light blue (30 °C) and dark blue (150 °C) curves in Figure 3(a), 0.3% of the nanopores contribute almost 100% of the total H_2 permeance. This percentage of permeable

https://dx.doi.org/10.1021/acsnano.0c09420
ACS Nano 2021, 15, 1727−1740

nanopores is 0.2% for CO_2 (orange and red curves) and is 0.01% for CH_4 (green and dark green curves) when the etching time is 20 (Figure 3(a)). As the etching time increases, the fraction of permeable nanopores increases, but remains lower than 15% even for an etching time of 80 (Figure 3(b), (c)). This trend is also illustrated in Figure 3(d)−(f), where the Lorenz curves shift to the upper left as the etching time increases. Generally, the permeance distribution of H_2 is the most even among those of the three gases considered due to its smallest kinetic diameter, while that of CH_4 is the most uneven due to its largest kinetic diameter.

As demonstrated in Figure 1(b) and Figure 2, a longer etching time t leads to a higher fraction of large and low-energy-barrier nanopores. Therefore, the theoretically predicted gas permeance of a nanopore ensemble is positively correlated with the etching time (Figure 4(a),(b)). At both 30 and 150 °C, H_2 exhibits the highest permeance per pore (averaged over the entire ensemble) for $20 < t < 80$, while the permeances per pore of CO_2 and CH_4 rank intermediate and lowest, respectively. The gas permeance exhibits much greater variance for a short etching time t, for which the probability of generating low-energy-barrier nanopores is low and has a large variance. On the other hand, as shown in Figure 4(c),(d), the theoretically predicted selectivities of the three gas separation pairs (CO_2/CH_4, H_2/CO_2, and H_2/CH_4) decrease as the etching time t increases. The selectivity decrease for $20 < t < 30$ is significant, decreasing from 10^3 to ∼10. Subsequently, the selectivity gradually decays to 1 as t increases further. Similar to the gas permeance, the selectivity also exhibits a high relative error for short etching times, partially reducing the precision of our estimation.

The high errors observed in the gas permeance and selectivity bring into question the reproducibility of the results, obtained both theoretically and experimentally. Fortunately, according to the central limit theorem, the standard deviation of the sample average of N independent and identically distributed random variables should scale as $N^{-1/2}$. This −1/2 scaling is confirmed in Figure 4(e) and (f), for the gas permeance per pore and for the selectivity, respectively. When the batch size N is as small as 100, the standard deviation of the sample average can be 10 times greater than the sample average (normalized standard deviation >10). Because both gas permeances and selectivities are non-negative quantities, the normal distribution does not seem to be the optimal choice for representing the uncertainty. However, according to the central limit theorem, as N increases, the sample average will approach a normal distribution. Therefore, we choose the normal distribution for consistency. If the $N^{-1/2}$ decay of the standard deviation persists as N increases further, we anticipate that the normalized standard deviation (or the relative error) should decrease to 5% when N reaches ∼4 million. Generating millions of nanopores *in silico* requires long real-world time for calculations, and $N = 10\,000$ is nearly the largest batch size that we can consider computationally. However, experimentally, if the graphene etching method is macroscopically scalable (*e.g.*, oxygen plasma), then, generating millions of nanopores in one graphene membrane is indeed possible. For example, Zhao *et al.* exposed graphene to oxygen plasma to increase the areal nanopore density to 5.7×10^{11} cm^{-2}.[7] At this areal density, 4 million nanopores require a membrane area of ∼700 μm^2, which has already been realized by reinforcing graphene with a highly porous supporting film.[13] Nevertheless, the inherent stochasticity associated with the pore size and shape distributions does exist and can partially account for the high variance of the experimentally measured gas permeances and selectivities carried out so far.[7,13]

Compared to the etching time, the effect of temperature on gas permeances and selectivities is more complex. Assuming that the translocation step is rate-determining ($K \approx K_{trans}$, for small nanopores), according to eq 1, the gas permeance is affected by temperature due to three terms: the adsorption term $H_{pore}(T)$, the Arrhenius term $\exp(-\Delta E^{\ddagger}/k_BT)$, and the kinetic term of $\sqrt{k_BT/2\pi m}$. $H_{pore}(T)$ is negatively correlated with temperature because it involves the heat of gas adsorption onto the graphene nanopore $\Delta E_{ads} < 0$ based on the expression $H_{pore}(T) = A_{pore} \exp(-\Delta E_{ads}/k_BT)$, where A_{pore} is the prefactor. If we neglect the kinetic term because its $T^{1/2}$ dependence is weaker than the exponential dependence in the other two terms, we find that the gas permeance is positively correlated with temperature if $\Delta E^{\ddagger} > -\Delta E_{ads}$ and is negatively correlated with temperature if $\Delta E^{\ddagger} < -\Delta E_{ds}$. On one hand, the heat of adsorption ΔE_{ads} is estimated to be −3.4, −11.1, and −8.0 kJ mol^{-1} for H_2, CO_2, and CH_4, respectively, based on our calculations using all-atomistic force fields (see Methods). On the other hand, when the etching time t = 30, the average energy barriers $\overline{\Delta E^{\ddagger}}$ for H_2, CO_2, and CH_4 are 2.8, 0.4, and 0.3 kJ mol^{-1} at 30 °C, respectively. This set of data is counterintuitive, because H_2 exhibits the highest average energy barrier although it is the smallest of the three gases considered. This is because the CO_2 and CH_4 permeances are dominated by nanopores with energy barriers close to zero, and all the other nanopores do not contribute to the sum in eq 5 because their energy barriers are too high.

The analysis above helps us interpret Figure 5, where we present the correlation of the gas permeances and the selectivities with temperature. For CO_2 and CH_4, $\Delta E^{\ddagger} \approx 0 < -\Delta E_{ads}$, and their permeances decrease as the temperature increases (Figure 5(a)). Because CO_2 is more adsorptive than CH_4, the permeance decrease of CO_2 is greater in magnitude. For H_2, $\Delta E^{\ddagger} \approx -\Delta E_{ads}$, and its permeance only slightly increases as a function of temperature (recall the $T^{1/2}$ term in eq 1). Consequently, the H_2/CO_2 and H_2/CH_4 selectivities increase as the temperature increases while the CO_2/CH_4 selectivity decreases (Figure 5(b)).

Next, we combine the data reported in Figure 4(a)−(d) to predict the permeance−selectivity Robeson plot in Figure 6. In the Robeson plot, the selectivity of gas A *vs* gas B is plotted on the y axis (assuming that gas A is more permeable), and the permeance per pore of gas A through a single nanopore or a nanopore ensemble is plotted on the x axis. The orange and red curves in Figure 6(a) represent the permeance−selectivity trade-off for H_2/CH_4 separation at 30 and 150 °C, respectively, where each data point corresponds to a nanopore ensemble generated with an etching time ranging from 20 to 80, in the direction from left to right on the x axis. Therefore, a short etching time corresponds to small pore sizes, a low gas permeance, and a high selectivity (top-left data points), while a long etching time corresponds to the opposite (bottom-right data points).

In order to evaluate the importance of considering the pore size and shape distributions, we also plotted the gas separation performances of the individual nanopores in the ensembles on the same Robeson plot (blue and green markers in Figure 6(a) for 30 and 150 °C, respectively). Note that all the data points of the individual nanopores lie above the ensemble-averaged

https://dx.doi.org/10.1021/acsnano.0c09420
ACS Nano 2021, 15, 1727−1740

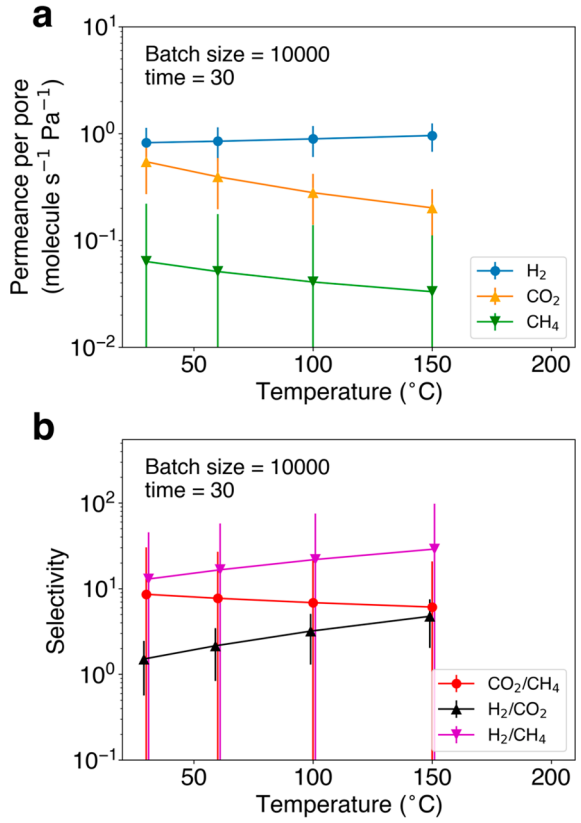

Figure 5. (a) Theoretically predicted temperature dependence of H_2, CO_2, and CH_4 permeances per pore. (b) Theoretically predicted temperature dependence of CO_2/CH_4, H_2/CO_2, and H_2/CH_4 selectivities. The etching time is 30 and the batch number is 10 000. The nanopore structures are assumed to be invariant as the temperature changes.

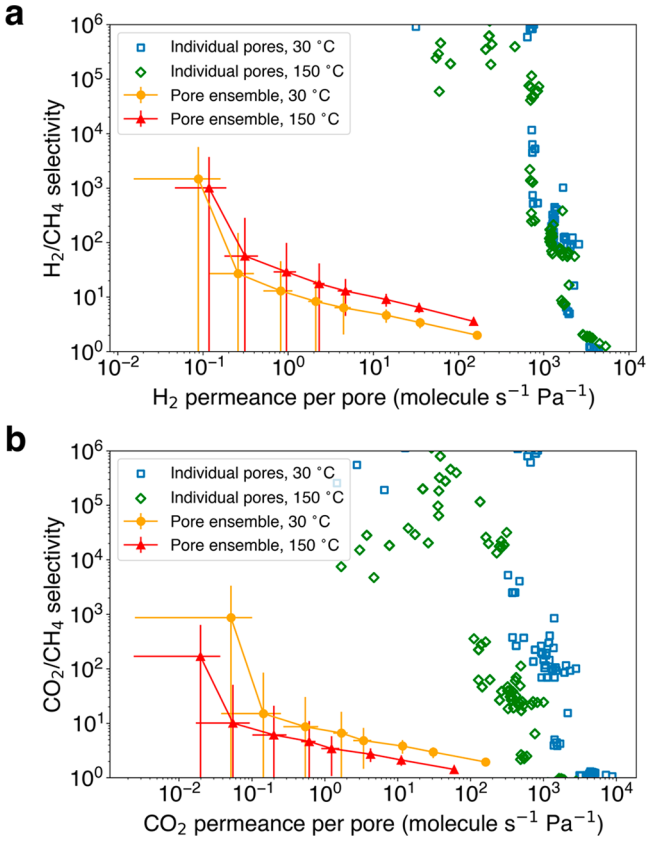

Figure 6. Theoretically predicted permeance−selectivity Robeson plot of (a) H_2/CH_4 separation and (b) CO_2/CH_4 separation at 30 and 150 °C. The orange and red curves represent the performance of nanopore ensembles, and the blue and green dots represent the performance of the individual nanopores.

curves (orange and red curves in Figure 6(a)). This gap between the individual nanopores and the nanopore ensembles highlights the need of taking the pore size and shape distributions into account. Most nanopores in an ensemble are basically not permeable (Figure 3), which reduces the average gas permeance. In Figure 6(a), a nanopore ensemble that yields a H_2/CH_4 selectivity of 10^3 permits a H_2 permeance per pore of only 10^{-1} molecule s^{-1} Pa^{-1}, which is four orders of magnitude lower compared to that of individual nanopores yielding the same selectivity. This gap in permeance shrinks as the selectivity target decreases, because the permeance distribution in a nanopore ensemble becomes more even as the etching time increases (Figure 3). The gap diminishes as the selectivity target approaches 1, when all the nanopores in an ensemble are too large to provide any selectivity. Features similar to those observed in Figure 6(a) are also observed in Figure 6(b), where the CO_2/CH_4 separation is evaluated. In spite of being similar in terms of the gap between the nanopore ensembles and the individual nanopores, the CO_2/CH_4 and H_2/CH_4 separations are different in terms of their temperature dependence. Increasing temperature shifts the H_2/CH_4 selectivity−permeance curve upward (orange to red, Figure 6(a)), but shifts the CO_2/CH_4 selectivity−permeance curve downward (orange to red, Figure 6(b)). This is a manifestation of the different temperature dependences of the permeances of the three gases, as reported in Figure 5(a).

It is important to note that our simulation results on the temperature dependence discussed above are based on the assumption that the nanopore structure remains unchanged as the temperature changes. However, temperature influences almost every aspect of an experimental measurement, and the actual experimental conditions may be more complex than those considered above by our theory. As shown in Figure 5(a), the permeances of CO_2 and CH_4 are predicted to decrease as the temperature increases, which contradicts the experimental findings.[7,13,16] To correct our theory in order to match the experimental findings, below, we propose a strategy.

Matching Theory with Experiments. In this section, we will compare our theoretically predicted gas permeances through nanoporous graphene membranes to experimentally measured ones.[7,26] For convenience, the 95% confidence interval of the theoretically predicted H_2, CO_2, and CH_4 permeances per pore and selectivities between the gases are reported in Table 1 (30 °C), Table 2 (100 °C), and Table 3 (150 °C) as functions of the etching time. The experimental data set used in this study was obtained by He *et al.*[26] and is reported in Table 4. Note that this data set was chosen because it has relatively low error and high reproducibility. The data set considered includes three types of nanoporous graphene samples, NG-1s, NG-2s, and NG-3s, fabricated by exposing pristine graphene grown by chemical vapor deposition (CVD) to 1, 2, and 3 s of oxygen plasma, respectively. Each membrane was tested to measure its H_2, CO_2, and CH_4 permeances at 30, 100, and 150 °C. Note that the nanopore edges are expected to be terminated by oxygen atoms or hydroxyl groups after oxygen plasma etching. However, the density and the positions

https://dx.doi.org/10.1021/acsnano.0c09420
ACS Nano 2021, 15, 1727−1740

Table 1. Predictions of Selectivities (S) and Permeances per Pore (K) of H_2, CO_2, and CH_4 at 30 °C through Graphene Nanopore Ensembles Generated Using Different Etching Times

	predicted selectivity			predicted permeance per pore (molecule s^{-1} Pa^{-1})		
etching time	$S(H_2/CH_4)$	$S(CO_2/CH_4)$	$S(H_2/CO_2)$	$K(H_2)$	$K(CO_2)$	$K(CH_4)$
20	1479.0 ± 1067.5	865.4 ± 642.2	1.7 ± 0.6	0.09 ± 0.02	0.05 ± 0.01	(6.0 ± 4.1) × 10^{-5}
21	132.8 ± 212.1	85.4 ± 137.1	1.6 ± 0.5	0.12 ± 0.03	0.07 ± 0.02	0.0009 ± 0.0014
22	25.5 ± 49.0	14.3 ± 27.6	1.8 ± 0.6	0.15 ± 0.03	0.09 ± 0.02	0.0060 ± 0.0114
26	22.3 ± 24.6	14.2 ± 15.7	1.6 ± 0.3	0.33 ± 0.05	0.21 ± 0.03	0.015 ± 0.016
27	16.3 ± 15.2	11.1 ± 10.4	1.5 ± 0.3	0.46 ± 0.06	0.31 ± 0.05	0.028 ± 0.026
28	14.9 ± 11.0	10.1 ± 7.5	1.5 ± 0.3	0.56 ± 0.06	0.38 ± 0.05	0.037 ± 0.027
30	13.0 ± 8.1	8.6 ± 5.4	1.5 ± 0.2	0.82 ± 0.08	0.54 ± 0.07	0.063 ± 0.039
31	11.8 ± 7.1	8.5 ± 5.1	1.4 ± 0.2	0.97 ± 0.09	0.70 ± 0.08	0.082 ± 0.048
32	10.0 ± 13.6	7.3 ± 10.0	1.4 ± 0.5	0.98 ± 0.20	0.71 ± 0.20	0.098 ± 0.132
35	8.3 ± 5.9	6.6 ± 4.7	1.3 ± 0.3	2.12 ± 0.32	1.69 ± 0.29	0.256 ± 0.178
40	6.3 ± 3.1	4.8 ± 2.4	1.3 ± 0.2	4.49 ± 0.50	3.41 ± 0.48	0.708 ± 0.334
45	5.6 ± 0.8	4.4 ± 0.6	1.3 ± 0.1	8.00 ± 0.31	6.22 ± 0.29	1.42 ± 0.19
50	4.6 ± 1.1	3.8 ± 0.9	1.2 ± 0.1	14.20 ± 0.98	11.66 ± 0.97	3.06 ± 0.71
52	4.1 ± 0.4	3.3 ± 0.3	1.2 ± 0.1	17.59 ± 0.50	14.31 ± 0.51	4.29 ± 0.37
55	3.7 ± 0.3	3.0 ± 0.2	1.2 ± 0.1	24.07 ± 0.61	19.57 ± 0.63	6.46 ± 0.48
60	3.4 ± 0.5	3.0 ± 0.4	1.2 ± 0.1	35.53 ± 1.69	30.88 ± 1.81	10.46 ± 1.39
70	2.5 ± 0.1	2.3 ± 0.1	1.1 ± 0.0	84.84 ± 1.29	79.03 ± 1.46	34.23 ± 1.17
80	2.0 ± 0.1	1.9 ± 0.1	1.0 ± 0.0	165.19 ± 4.32	160.98 ± 5.08	83.01 ± 4.25

Table 2. Predictions of Selectivities (S) and Permeances per Pore (K) of H_2, CO_2, and CH_4 at 100 °C through Graphene Nanopore Ensembles Generated Using Different Etching Times

	predicted selectivity			predicted permeance per pore (molecule s^{-1} Pa^{-1})		
etching time	$S(H_2/CH_4)$	$S(CO_2/CH_4)$	$S(H_2/CO_2)$	$K(H_2)$	$K(CO_2)$	$K(CH_4)$
20	1127.5 ± 787.4	291.9 ± 211.6	3.9 ± 1.3	0.10 ± 0.02	0.03 ± 0.01	(9,2 ± 6.2) × 10^{-5}
21	178.1 ± 243.1	51.4 ± 70.8	3.5 ± 1.1	0.13 ± 0.02	0.04 ± 0.01	0.0008 ± 0.0010
22	46.0 ± 85.8	11.8 ± 22.1	3.9 ± 1.1	0.18 ± 0.03	0.05 ± 0.01	0.0038 ± 0.0071
26	38.2 ± 39.9	11.0 ± 11.6	3.5 ± 0.7	0.37 ± 0.04	0.11 ± 0.02	0.0098 ± 0.0102
27	27.9 ± 25.2	9.0 ± 8.2	3.1 ± 0.6	0.51 ± 0.05	0.16 ± 0.02	0.018 ± 0.016
28	25.2 ± 17.9	8.0 ± 5.8	3.1 ± 0.5	0.61 ± 0.06	0.19 ± 0.03	0.024 ± 0.017
30	21.9 ± 13.3	6.9 ± 4.2	3.2 ± 0.5	0.89 ± 0.07	0.28 ± 0.03	0.041 ± 0.025
31	19.6 ± 11.3	6.8 ± 4.0	2.9 ± 0.4	1.04 ± 0.08	0.36 ± 0.04	0.053 ± 0.030
32	16.9 ± 22.4	5.8 ± 7.9	2.9 ± 0.9	1.06 ± 0.19	0.37 ± 0.10	0.063 ± 0.083
35	13.5 ± 9.4	5.2 ± 3.7	2.6 ± 0.6	2.21 ± 0.30	0.86 ± 0.15	0.164 ± 0.111
40	10.1 ± 4.8	3.8 ± 1.9	2.6 ± 0.5	4.57 ± 0.46	1.74 ± 0.25	0.453 ± 0.210
45	8.8 ± 1.2	3.5 ± 0.5	2.6 ± 0.2	8.01 ± 0.28	3.14 ± 0.15	0.909 ± 0.120
50	7.2 ± 1.7	3.0 ± 0.7	2.4 ± 0.2	14.03 ± 0.90	5.96 ± 0.50	1.96 ± 0.45
52	6.3 ± 0.6	2.7 ± 0.2	2.4 ± 0.1	17.30 ± 0.46	7.30 ± 0.26	2.74 ± 0.24
55	5.7 ± 0.4	2.4 ± 0.2	2.3 ± 0.1	23.48 ± 0.55	9.99 ± 0.33	4.13 ± 0.30
60	5.2 ± 0.7	2.4 ± 0.3	2.2 ± 0.2	34.44 ± 1.54	15.79 ± 0.95	6.67 ± 0.88
70	3.7 ± 0.1	1.9 ± 0.1	2.0 ± 0.0	80.34 ± 1.16	40.58 ± 0.77	21.77 ± 0.74
80	2.9 ± 0.2	1.6 ± 0.1	1.8 ± 0.1	154.19 ± 3.86	83.38 ± 2.70	52.74 ± 2.69

of the oxygen-containing termination groups cannot be easily predicted or modeled. Moreover, the additional rotational degrees of freedom contributed by the termination groups could significantly expand the phase space of nanopore−gas interactions, boosting the computational cost. In fact, if the nanopore−gas interactions remain mainly dispersive and not electrostatic, *i.e.*, if we assume that the oxygen-containing termination groups are sparse, which results in weak gas−nanopore electrostatic interactions, our calculations without edge termination can still effectively accommodate for the edge termination groups by considering them as part of the graphene lattice. This is likely the case for oxygen plasma-etched nanopores.[26] Therefore, for simplicity and efficiency, we assume that the nanopores are not terminated.

As shown in Table 4, for each membrane considered, the experimentally measured H_2/CO_2 selectivity increases as the temperature increases, while the CO_2/CH_4 selectivity shows the opposite trend. These trends are correctly predicted by our theory (Figure 5(b)). However, our theoretical prediction in Figure 5(b) fails to match the experimentally observed decrease in the H_2/CH_4 selectivity with increasing temperature (Table 4). As indicated earlier, Figure 5 was derived based on the assumption that the nanopore size remains unchanged as the temperature increases, an assumption that could be relaxed in order to reproduce realistic experimental conditions. Specifically, by relaxing this assumption, we could assign different etching times to the same graphene membrane at different temperatures. For example, as listed in the first entry in Table 4, the H_2/CH_4, CO_2/CH_4, and H_2/CO_2 selectivities

https://dx.doi.org/10.1021/acsnano.0c09420
ACS Nano 2021, 15, 1727−1740

Table 3. Predictions of Selectivities (S) and Permeances per Pore (K) of H_2, CO_2, and CH_4 at 150 °C through Graphene Nanopore Ensembles Generated Using Different Etching Times

	predicted selectivity			predicted permeance per pore (molecule s^{-1} Pa^{-1})		
etching time	$S(H_2/CH_4)$	$S(CO_2/CH_4)$	$S(H_2/CO_2)$	$K(H_2)$	$K(CO_2)$	$K(CH_4)$
20	1007.0 ± 688.9	168.5 ± 120.1	6.0 ± 1.9	0.12 ± 0.02	0.02 ± 0.01	(1.1 ± 0.8) × 10^{-4}
21	205.6 ± 251.4	38.6 ± 47.7	5.3 ± 1.6	0.15 ± 0.02	0.03 ± 0.01	(7.3 ± 8.8)E-4
22	63.3 ± 114.8	10.7 ± 19.5	5.9 ± 1.6	0.20 ± 0.03	0.03 ± 0.01	0.003 ± 0.006
26	51.0 ± 51.4	9.6 ± 9.8	5.3 ± 1.0	0.41 ± 0.04	0.08 ± 0.01	0.008 ± 0.008
27	37.3 ± 32.8	8.1 ± 7.1	4.6 ± 0.8	0.55 ± 0.05	0.12 ± 0.02	0.015 ± 0.013
28	33.4 ± 23.1	7.1 ± 5.0	4.7 ± 0.8	0.66 ± 0.06	0.14 ± 0.02	0.020 ± 0.014
30	28.9 ± 17.2	6.1 ± 3.7	4.8 ± 0.7	0.96 ± 0.07	0.20 ± 0.02	0.033 ± 0.020
31	25.8 ± 14.5	6.1 ± 3.5	4.2 ± 0.6	1.11 ± 0.08	0.26 ± 0.03	0.043 ± 0.024
32	22.5 ± 29.3	5.2 ± 6.9	4.3 ± 1.4	1.15 ± 0.19	0.27 ± 0.07	0.051 ± 0.066
35	17.5 ± 11.9	4.6 ± 3.2	3.8 ± 0.8	2.32 ± 0.29	0.61 ± 0.11	0.13 ± 0.09
40	12.9 ± 6.0	3.4 ± 1.6	3.8 ± 0.6	4.72 ± 0.45	1.25 ± 0.18	0.36 ± 0.17
45	11.2 ± 1.5	3.0 ± 0.4	3.7 ± 0.2	8.19 ± 0.28	2.23 ± 0.10	0.73 ± 0.10
50	9.0 ± 2.1	2.7 ± 0.7	3.3 ± 0.3	14.21 ± 0.87	4.26 ± 0.36	1.58 ± 0.36
52	7.9 ± 0.7	2.4 ± 0.2	3.3 ± 0.1	17.47 ± 0.44	5.22 ± 0.19	2.20 ± 0.19
55	7.1 ± 0.5	2.2 ± 0.2	3.3 ± 0.1	23.59 ± 0.53	7.14 ± 0.24	3.32 ± 0.24
60	6.4 ± 0.9	2.1 ± 0.3	3.1 ± 0.2	34.47 ± 1.48	11.28 ± 0.68	5.36 ± 0.70
70	4.5 ± 0.2	1.7 ± 0.1	2.7 ± 0.1	79.27 ± 1.11	29.03 ± 0.56	17.45 ± 0.59
80	3.6 ± 0.2	1.4 ± 0.1	2.5 ± 0.1	150.80 ± 3.68	59.85 ± 1.95	42.24 ± 2.15

Table 4. Experimentally Measured H_2/CH_4, CO_2/CH_4, and H_2/CO_2 Selectivities (S) in Ref 26[a]

condition		measured selectivity				fitted selectivity		
membrane	temperature (°C)	$S(H_2/CH_4)$	$S(CO_2/CH_4)$	$S(H_2/CO_2)$	best fit of etching time	$S(H_2/CH_4)$	$S(CO_2/CH_4)$	$S(H_2/CO_2)$
NG-1s	30	15.9 ± 3.8	8.7 ± 0.7	1.8 ± 0.3	28	14.9 ± 11.0	10.1 ± 7.5	1.5 ± 0.3
NG-1s	100	14.1 ± 7.3	5.9 ± 2.3	2.3 ± 0.3	35	13.5 ± 9.4	5.2 ± 3.7	2.6 ± 0.6
NG-1s	150	10.1 ± 3.0	3.7 ± 0.7	2.7 ± 0.3	45	11.2 ± 1.5	3.0 ± 0.4	3.7 ± 0.2
NG-2s	30	9.2 ± 1.9	6.7 ± 2.9	1.5 ± 0.4	35	8.3 ± 5.9	6.6 ± 4.7	1.3 ± 0.3
NG-2s	100	8.2 ± 1.6	3.5 ± 1.1	2.4 ± 0.3	45	8.8 ± 1.2	3.5 ± 0.5	2.6 ± 0.2
NG-2s	150	7.6 ± 1.7	2.6 ± 0.6	3.0 ± 0.1	52	7.9 ± 0.7	2.4 ± 0.2	3.3 ± 0.1
NG-3s	30	5.0 ± 1.1	3.1 ± 0.8	1.6 ± 0.3	50	4.6 ± 1.1	3.8 ± 0.9	1.2 ± 0.1
NG-3s	100	5.6 ± 1.9	2.2 ± 0.5	2.5 ± 0.3	60	5.2 ± 0.7	2.4 ± 0.3	2.2 ± 0.2
NG-3s	150	4.9 ± 0.9	1.7 ± 0.1	2.8 ± 0.3	70	4.5 ± 0.2	1.7 ± 0.1	2.7 ± 0.1

[a]Each membrane−temperature combination was matched to an etching time that best reproduces the experimental selectivities.

are 15.9 ± 3.8, 8.7 ± 0.7, and 1.8 ± 0.3, respectively, for membrane NG-1s at 30 °C. As shown in Table 1, we predict that an etching time of 28 corresponds to selectivities of 14.9 ± 11.0, 10.1 ± 7.5, and 1.5 ± 0.3, which yields the closest match to the experimentally measured values (equal weights are assigned to the three selectivities). Similarly, we can find the etching times that best match the experimentally measured selectivities for each membrane at each temperature (rows 2−9 in Table 4). The uncertainty of the theoretically predicted H_2/CH_4 and CO_2/CH_4 selectivities for short etching times (t < 40) makes the fitting more challenging. However, Table 1, Table 2, and Table 3 show that the selectivity decrease as a function of temperature is smooth, thereby corroborating the reliability of our theoretical predictions. The fit does a reasonably good job in matching the experimental selectivities (Table 4). In addition, the fit successfully confirms the intuitive fact that, at the same temperature, a nanoporous graphene membrane exposed to a longer duration of oxygen plasma is always matched to a longer etching time t (*e.g.*, 50 > 35 > 28 for NG-3s, NG-2s, and NG-1s at 30 °C).

This fit leads to the following important finding: for the same graphene membrane, the fitted etching time t is longer at a higher temperature of permeation measurement (not the temperature of graphene etching) than that at a lower temperature. Note that the fitted etching time is only a one-degree-of-freedom representation of the underlying pore size distribution, and therefore, the nanopores are effectively larger at a higher temperature of permeation measurement. This effective pore size expansion is also observed in other experimental data sets reported in ref 7, ref 16, and ref 27 (see SI Section S3 for more details, where the effect of ozone treatment is also investigated). This phenomenon is inconsistent with our previous assumption in Figure 5 and Figure 6 that the nanopore structure does not depend on temperature. One could explain this phenomenon by arguing that the graphene nanopores expand due to the contraction of the graphene lattice. However, the thermal expansion coefficient of graphene at room temperature is only −7 × 10^{-6} K^{-1},[28] suggesting that the thermally induced expansion of a graphene nanopore is minimal.

In order to resolve this apparent contradiction, we hypothesize that under the experimental conditions used, the graphene nanopores are partially clogged, likely by some airborne hydrocarbon contaminants. It is known that the adsorption of airborne hydrocarbons on graphitic surfaces renders them more hydrophobic.[29,30] Heat treatment at 150 °C has been confirmed to be effective in alleviating the clogging,[7] but is not able to fully remove the contaminants,

https://dx.doi.org/10.1021/acsnano.0c09420
ACS Nano 2021, 15, 1727−1740

Table 5. Experimentally Measured H_2, CO_2, and CH_4 Permeances Reported in Ref 26 and Theoretical Predictions of the Gas Permeances Using the Best Fit of Etching Time in Table 4

condition		measured permeance (GPU)			best fit of etching time	predicted permeance (GPU)			average factor of permeance under-estimation
membrane	temperature (°C)	H_2	CO_2	CH_4		H_2	CO_2	CH_4	
NG-1s	30	3130	1765	205	28	18.0 ± 1.9	12.2 ± 1.6	1.2 ± 0.8	163
NG-1s	100	1.32×10^4	5782	1112	35	71.2 ± 9.7	27.7 ± 4.8	5.3 ± 3.6	202
NG-1s	150	2.17×10^4	7931	2222	45	263.8 ± 9.0	71.8 ± 3.2	23.5 ± 3.2	96
NG-2s	30	1.73×10^4	1.20×10^4	1963	35	189.1 ± 28.5	150.8 ± 25.9	22.8 ± 15.9	86
NG-2s	100	4.47×10^4	1.91×10^4	5522	45	714.6 ± 25.0	280.1 ± 13.4	81.1 ± 10.7	66
NG-2s	150	6.69×10^4	2.25×10^4	8928	52	1559 ± 39	476.7 ± 16.9	196.3 ± 16.9	46
NG-3s	30	3.23×10^4	2.00×10^4	6830	50	1548 ± 107	1271 ± 106	333.6 ± 77.4	19
NG-3s	100	8.06×10^4	3.40×10^4	1.59×10^4	60	3755 ± 168	1722 ± 104	727.3 ± 96.0	21
NG-3s	150	1.29×10^5	4.73×10^4	2.76×10^4	70	8643 ± 121	3165 ± 61	1903 ± 64	15

because a single to few layers of the contaminant molecules are sufficient to clog the nanopores. Our partial clogging hypothesis can also help rationalize the following three discrepancies between theory and experiment.

First, the effective thermal expansion of nanopores can be interpreted as a result of the partial desorption of the contaminants from the nanopore. In other words, the clogging of the nanopores is alleviated at a higher temperature. A prerequisite for this explanation is that the original, unclogged graphene nanopores should be larger than those fitted by our theoretical prediction. Reference 26 presents the pore diameter distributions of graphene membranes NG-1s and NG-3s obtained by high-resolution transmission electron microscopy (HR-TEM). Membrane NG-1s contains a long tail of nanopores with diameters over 2 nm, and the tail of the pore diameter distribution of membrane NG-3s extends to over 3 nm. In contrast, the predicted pore diameter distribution does not extend over 1 nm, even for the longest etching time investigated, t = 80 (SI Section S4). If the large nanopores generated in the experiments are completely free from clogging, they would exhibit a total CO_2 permeance 6600 times higher than that measured.[26] The long pore size tail observed in ref 26 could also be partially attributed to nanopore merging during HR-TEM imaging, but our statement remains valid because the average pore diameter observed by HR-TEM is greater than our theoretically fitted value.

Second, the effective thermal expansion of the nanopores explains why the experimentally measured gas permeances almost always increase as the temperature increases. At a higher temperature, CO_2 and CH_4 adsorb less, reducing their gas permeances (Figure 5(a)). However, the permeance increase due to the effective thermal expansion of the nanopores *via* the desorption of contaminants is much more significant. In this case, we need to carefully revisit the definition of the energy barrier (or the activation energy) derived from the experimental data. If the effective pore size changes at different temperatures, it follows that the apparent "energy barrier" derived by fitting the Arrhenius equation to the gas permeance as a function of temperature actually contains contributions from both the intrinsic energy barrier for a given pore size $\Delta E^{\ddagger}$ and the desorption of the contaminants. In fact, the latter is likely to be dominant because the average energy barrier of a temperature-invariant nanopore ensemble is close to zero, much lower than 10 to 30 kJ mol^{-1} measured in the experimental studies.[7,13,16] Without the nanopore clogging by the contaminants, He *et al.* predict that 99.9% of the CO_2 permeance through NG-1s in ref 26 was contributed by nanopores larger than 5.8 Å in diameter, whose activation energies for CO_2 are close to 0, directly contradicting the experimentally measured CO_2 apparent energy barrier of 13.8 kJ mol^{-1}. This hypothesis also explains why in those studies the apparent "energy barriers" are very similar across various nanoporous graphene membranes fabricated by different methods, because they are strongly affected by the universal thermal behavior of the contaminants.

Finally, the partial clogging hypothesis helps explain why our theory underpredicts the gas permeances compared to the experimental measurements reported in ref 26. As shown in Table 4, we attempt to find the etching time t that best matches the selectivities between theory and experiment, instead of the gas permeances. In fact, the selectivities and the gas permeances cannot be matched simultaneously. As shown in Table 5, when the etching time t is fitted to match the selectivity data, our theory underpredicts the gas permeances by 15−202 times. The predicted permeance (in gas permeation units, *i.e.*, GPU) equals the predicted permeance per pore (in molecule s^{-1} Pa^{-1}) times the experimentally measured areal defect density in the graphene membranes using Raman spectroscopy, with an appropriate unit conversion. This significant underprediction cannot be easily explained without the partial clogging hypothesis. Note that the clogging was not considered in our original theoretical model. When clogging is accounted for and reduces the open nanopore area, in order to maintain the same selectivity through the nanopore ensemble, we need to increase the etching time t to compensate for the area loss. As shown in Figure 1(b), the tail in the pore size distribution elongates as t increases. As a result, taking pore clogging into consideration leads to an increase in the fraction of low-energy-barrier nanopores in the nanopore ensemble. In other words, we underestimate the etching time t by fitting our model to the

https://dx.doi.org/10.1021/acsnano.0c09420
ACS Nano 2021, 15, 1727−1740

selectivity data because of clogging, which leads to an underestimation of the number of permeable nanopores and an underestimation of the gas permeances. As reported in the last column in Table 5, the magnitude of our underestimation decreases as the nanopore size increases. This makes intuitive sense because larger nanopores are less affected by contaminants, which likely clog the nanopores from the nanopore edges.

Other hypotheses that can explain the effective pore size expansion include (1) the pore size distributions generated by our KMC algorithm do not match experimental ones and (2) the effective pore size expansion is induced by the more mobile termination groups (*e.g.*, carbonyl groups) at a higher temperature. Regarding (1), the pore size distribution generated by our KMC algorithm can reproduce the apparent energy barriers observed experimentally (SI Table S7), suggesting that the difference between the experimental and theoretically derived pore size distributions is minor. Regarding (2), the graphene nanopores in ref 16 and ref 27 were formed during CVD in a reductive atmosphere and, therefore, were not likely terminated by large, oxygen-containing groups. Nevertheless, these nanopores still exhibit the effective pore size expansion as the temperature increases (SI Tables S5 and S6), indicating that the termination groups alone cannot account for the effective pore size expansion.

CONCLUSIONS

This paper formulated a theoretical framework that predicts the pore size and shape distributions of nanopore ensembles generated by etching, as well as the gas permeances of H_2, CO_2, and CH_4 through these nanopore ensembles. We showed that a small fraction of low-energy-barrier nanopores contribute the majority of the total gas permeances through a nanopore ensemble that sieves gases. We quantitatively predict the increase of the gas permeances and the decrease of the gas selectivities as the etching time of graphene increases. Assuming that the nanopore structure is independent of temperature given the small thermal expansion coefficient of graphene, our theory predicts that the CO_2 and CH_4 permeances decrease and the H_2 permeance increases as the temperature increases. The CO_2 and CH_4 permeance predictions contradict the experimental results, where all the experimental gas permeances are increasing functions of temperature. In order to explain this contradiction, we fitted our theoretical model to match the experimentally measured H_2/CH_4, CO_2/CH_4, and H_2/CO_2 selectivities and find that the nanopores effectively expand at a higher temperature. We hypothesized that under typical experimental conditions the graphene nanopores are partially clogged by hydrocarbon contaminants and that the contaminants desorb as the temperature increases. An important implication of this hypothesis is that the apparent "energy barriers" directly derived from the experimentally measured gas permeances can be significantly affected by the thermal behavior of the contaminants. Therefore, a high apparent "energy barrier" does not necessarily prove the existence of angstrom-scale graphene nanopores. On the bright side, another implication of our hypothesis is that it may not be necessary to reduce the graphene nanopore size to the angstrom scale in order to attain a high selectivity, because clogging by contaminants effectively reduces the pore size. In the future, experimental research can be conducted to verify the effect of hydrocarbon contaminants on gas permeances by, for example, deliberately decorating graphene membranes using strongly adsorptive hydrocarbons. In addition, the effect of edge termination in graphene nanopores can be evaluated to better model the typical oxygen plasma etching method.

We believe that our article provides an important theoretical benchmark for future experimental gas permeation measurements through graphene membranes. The experimentally measured selectivities can be compared with Tables 1−3 to find the best-fitted etching time, and the pore size distribution can be inferred from the etching time according to Figure 1(b).

METHODS

Kinetic Monte Carlo Nanopore Generation. The major steps involved in the KMC simulation are presented in Figure 1(a). Starting from a point defect in a pristine graphene lattice containing 12 × 12 unit cells, carbon atoms were etched away sequentially. The 12 × 12 graphene lattice is large enough to contain the nanopores considered in this work. The rate of a carbon atom being removed is related to its nearby edge configuration. The energy barrier E_a for removing a single carbon atom is 2.30 eV at a zigzag edge, 2.28 eV at an armchair edge, and 1.03 eV for a singly bonded atom.[14] The corresponding etching rate r is computed using an Arrhenius-type equation: $r = \nu \exp(-E_a/k_BT)$, where ν is a prefactor related to the etchant concentration. In this work, ν is chosen to be 10^{13} s^{-1}. The value of ν is arbitrary, because it does not affect the pore size and shape distributions generated using the KMC algorithm. In fact, the etching time t can be rescaled if ν is assumed to be different. The temperature was assumed to be 500 °C to match the experimental graphene etching condition in ref 31. The nanopore ensembles predicted using the KMC algorithm are insensitive to temperature.[14] This is likely because the energy barriers for removing a carbon atom at a zigzag edge or at an armchair edge are similar, making the effect of temperature less important. When multiple choices exist about which carbon atom to etch, we implemented the Gillespie algorithm to randomly select one of them. The probability of a carbon atom being etched is proportional to its respective etching rate r.

Among the 500 000 nanopores generated using the KMC algorithm, many of them are identical to one another. Two nanopores are considered to be the same if the adjacency matrices of their respective antimolecules, augmented to include bond orientations, are isomorphic.[14] The antimolecule of a nanopore is the collection of the carbon atoms removed during etching. For additional details and for the KMC simulation and nanopore counting code, interested readers are referred to ref 14. One nanopore isomer was evaluated only once to calculate its permeance to avoid calculational redundancy. As the pore size increases, the number of isomers significantly increases, leading to a long calculation time. To make the calculation more tractable, the number of nanopores generated was reduced to 100 000 for etching time $t \geq 60$.

Permeance Prediction. The gas permeance per pore K through a nanopore was calculated using eqs 1−4. In eq 1, H_{pore} (average number of gas molecules adsorbed to the pore mouth per unit bulk pressure), L (the characteristic length of the adsorbed state at the pore mouth), $-\Delta S^{\ddagger}$ (the entropy barrier), and $\Delta E^{\ddagger}$ (the energy barrier) all depend on the force fields used to simulate graphene and the three gases considered (H_2, CO_2, CH_4). In our simulations, all-atom force fields were used to describe the atomic interactions, where all the molecules were assumed to be rigid in order to reduce computational cost. As shown in our previous study,[11] enforcing rigidity on all the molecules leads to a slight underprediction of the gas permeance. Specifically, we overpredict the entropy barrier $-\Delta S^{\ddagger}$ because the vibrational degrees of freedom are frozen, reducing the number of microstates at the transition state. Recall that nonbonded interactions include Lennard-Jones potentials and point-charge-based electrostatic potentials. We adopted the three-site model for H_2,[32] the transferable potential for phase equilibria (TraPPE) force field for CO_2,[33] and the all-atom-optimized potentials for liquid simulations (OPLS-AA model) for CH_4.[34] The carbon atoms in the graphene

https://dx.doi.org/10.1021/acsnano.0c09420
ACS Nano 2021, 15, 1727−1740

lattice were modeled as uncharged atoms using the Lennard-Jones parameters reported by Cheng and Steele.[35] The edge carbon atoms were not terminated by any functional groups. In reality, the edge termination depends on the etching method, and the nanopore could be terminated by hydrogen, oxygen, or hydroxyl groups or left unterminated. If the nanopore edge is highly polarized (*e.g.*, a large number of oxygen heteroatoms), our theory tends to underpredict the permeances of gases with a dipole moment (*e.g.*, H_2O) or a quadrupole moment (CO_2), which is the case for ozone-treated nanopores.[7] This underprediction is discussed in SI Section S3. The cutoff distance for the Lennard-Jones interactions was chosen to be 1.2 nm. Geometric-mean combining rules were implemented to describe the nonbonded interactions between different atoms.

The selected all-atom force fields allowed us to calculate the interaction energy $E(r,\phi,z,\vec{\theta})$ between the gas molecule and the single-layer graphene sheet with one nanopore generated by the KMC algorithm, where (r,ϕ,z) and $\vec{\theta}$ are the position (cylindrical coordinate) and the orientation of the gas molecule relative to the graphene surface, respectively. In this work, we define the normal direction to the graphene basal plane as the z direction. In order to calculate the Helmholtz free energy profile of pore crossing $A(z)$, we first calculated the canonical partition function profile $Q(z)$ as follows:[11]

$$Q(z) = \frac{\int \mathrm{d}\vec{\theta} \iint_{\Omega} r \,\mathrm{d}r \,\mathrm{d}\phi \exp\left[-\frac{E(r,\phi,z,\vec{\theta})}{k_B T}\right]}{\int \mathrm{d}\vec{\theta} \iint_{\Omega} r \,\mathrm{d}r \,\mathrm{d}\phi}$$

where Ω is the nanopore area around the nanopore center with a radius of 0.4 nm. This nanopore area is sufficiently large to include relevant nanopore−gas interactions because the diameters of the nanopores considered here rarely exceed 0.8 nm. We then calculated the Helmholtz free energy profile using the well-known statistical mechanical relation $A(z) = -k_B T \ln Q(z)$.[36] The Helmholtz free energy barrier is then calculated as $\Delta A^{\ddagger} = \max(A(z)) - \min(A(z))$. The entropy barrier ($-\Delta S^{\ddagger}$) and the energy barrier ($\Delta E^{\ddagger}$) are then calculated by linearly fitting $\Delta A^{\ddagger}(T) = \Delta E^{\ddagger} - T\Delta S^{\ddagger}$ to the temperature T.

The full width at half-maximum L of the canonical partition function of the gas−pore system $Q(z)$ is derived as follows:[11]

$$L = \frac{\int_0^{z_{\max}} Q(z)\,\mathrm{d}z}{\max(Q(z))}$$

where $z_{\max}$ is the thickness of the adsorption layer. Note that we chose $z_{\max} = 0.5$ nm, where the density of the gas molecules approaches the bulk value. The average number of gas molecules adsorbed at the pore mouth per unit bulk pressure H_{pore} was calculated as follows:

$$H_{\mathrm{pore}}(T) = \frac{\Omega \int_0^{z_{\max}} Q(z)\,\mathrm{d}z}{k_B T Q(z \to \infty)}$$

Note that in the last equation, we calculated the number of gas molecules near the nanopore (the numerator) relative to the bulk gas density (the denominator). The heat of adsorption ΔE_{ads} was derived by fitting $H_{\mathrm{pore}}(T) = A_{\mathrm{pore}} \exp(-\Delta E_{\mathrm{ads}}/k_B T)$ to the temperature.

In practice, we need to discretize the phase space $(r,\phi,z,\vec{\theta})$ to approximate the integrals by sums. Specifically, the r space was divided into grids of 0.013 nm, the ϕ space was divided into grids of 18°, the z space was divided into grids of 0.033 nm, and the θ space was discretized by randomly sampling 10 three-dimensional directions per position (r,ϕ,z). The grid sizes in the r, ϕ, and z directions and the number of randomly sampled directions in $\vec{\theta}$ were selected to ensure convergence of the Helmholtz free energy barrier $\Delta A^{\ddagger}$. Additional details about the convergence are provided in SI Section S6.

Equations 2 and 3 involve additional parameters, including the two correction factors δ and γ, the areal density of gas molecules adsorbed on the graphene surface per unit bulk pressure H_{surf}, and the equivalent pore diameter D_p. According to our previous study,[4] $\delta = \left(1 - \frac{D_m}{D_p}\right)^{\alpha}$, where D_m is the kinetic diameter of the gas and α is a gas-dependent exponent (4.6 for H_2 and CO_2 and 3.7 for CH_4). Because the graphene nanopores are not perfectly circular, we approximated the equivalent pore diameter $D_p = \sqrt{\frac{4n}{\pi\rho}}$, where n is the pore size (number of removed carbon atoms) and ρ is the areal density of the carbon atoms in graphene, 3.82×10^{19} m^{-2}. The surface adsorption term H_{surf} can be derived in a similar way as H_{pore}, except that the graphene sheet has no nanopore. Note that the correction factor $\gamma = \gamma(T, D_p)$ in eq 3 does not yet have an analytical expression due to the complex gas−gas collisions and gas−pore interactions. Empirically, we interpolated the γ values based on our previous study in ref 4. Typically, γ is on the order of 0.05−0.10 regardless of gas type or temperature. Fortunately, K_{trans} (calculated using eq 1) is typically much lower than $K_{\mathrm{direct}} + K_{\mathrm{surface}}$ (calculated using eqs 2 and 3), and therefore, $K \approx K_{\mathrm{trans}}$ (eq 4). Consequently, our final prediction of the gas permeance is quite insensitive to the parameters in eqs 2 and 3.

ASSOCIATED CONTENT

Supporting Information

The Supporting Information is available free of charge at https://pubs.acs.org/doi/10.1021/acsnano.0c09420.

Section S1: Importance of the entropy barrier; Section S2: Derivation of the average energy barrier; Section S3: Matching the theory to other experimental data sets; Section S4: Predicted pore diameter distribution; Section S5: Comparison of apparent energy barriers between experiments and theory; Section S6: Convergence test of the phase space discretization (PDF)

AUTHOR INFORMATION

Corresponding Author

Daniel Blankschtein − *Department of Chemical Engineering, Massachusetts Institute of Technology, Cambridge, Massachusetts 02139, United States;* orcid.org/0000-0002-7836-415X; Email: dblank@mit.edu

Authors

Zhe Yuan − *Department of Chemical Engineering, Massachusetts Institute of Technology, Cambridge, Massachusetts 02139, United States;* orcid.org/0000-0002-7627-2980

Ananth Govind Rajan − *Department of Chemical Engineering, Indian Institute of Science, Bengaluru, Karnataka 560012, India;* orcid.org/0000-0003-2462-0506

Guangwei He − *Department of Chemical Engineering, Massachusetts Institute of Technology, Cambridge, Massachusetts 02139, United States*

Rahul Prasanna Misra − *Department of Chemical Engineering, Massachusetts Institute of Technology, Cambridge, Massachusetts 02139, United States;* orcid.org/0000-0001-5574-2384

Michael S. Strano − *Department of Chemical Engineering, Massachusetts Institute of Technology, Cambridge, Massachusetts 02139, United States;* orcid.org/0000-0003-2944-808X

Complete contact information is available at: https://pubs.acs.org/10.1021/acsnano.0c09420

Notes

The authors declare no competing financial interest.

https://dx.doi.org/10.1021/acsnano.0c09420
ACS Nano 2021, 15, 1727−1740

ACKNOWLEDGMENTS

We acknowledge financial support from the National Science Foundation (NSF) grant number CBET-1907716. For computational resources, this work used the Extreme Science and Engineering Discovery Environment (XSEDE),[37] which is supported by NSF grant number ACI-1548562. G.H. acknowledges the funding from Swiss National Science Foundation (grant number P400P2_186682).

REFERENCES

(1) Wang, L.; Boutilier, M. S. H.; Kidambi, P. R.; Jang, D.; Hadjiconstantinou, N. G.; Karnik, R. Fundamental Transport Mechanisms, Fabrication and Potential Applications of Nanoporous Atomically Thin Membranes. *Nat. Nanotechnol.* **2017**, *12* (6), 509−522.

(2) Yoo, B. M.; Shin, J. E.; Lee, H. D.; Park, H. B. Graphene and Graphene Oxide Membranes for Gas Separation Applications. *Curr. Opin. Chem. Eng.* **2017**, *16*, 39−47.

(3) Moghadam, F.; Park, H. B. Two-Dimensional Materials: An Emerging Platform for Gas Separation Membranes. *Curr. Opin. Chem. Eng.* **2018**, *20*, 28−38.

(4) Yuan, Z.; Misra, R. P.; Rajan, A. G.; Strano, M. S.; Blankschtein, D. Analytical Prediction of Gas Permeation through Graphene Nanopores of Varying Sizes: Understanding Transitions across Multiple Transport Regimes. *ACS Nano* **2019**, *13* (10), 11809−11824.

(5) Jiang, D.; Cooper, V. R.; Dai, S. Porous Graphene as the Ultimate Membrane for Gas Separation. *Nano Lett.* **2009**, *9* (12), 4019−4024.

(6) Robeson, L. M. The Upper Bound Revisited. *J. Membr. Sci.* **2008**, *320* (1−2), 390−400.

(7) Zhao, J.; He, G.; Huang, S.; Villalobos, L. F.; Dakhchoune, M.; Bassas, H.; Agrawal, K. V. Etching Gas-Sieving Nanopores in Single-Layer Graphene with an Angstrom Precision for High-Performance Gas Mixture Separation. *Sci. Adv.* **2019**, *5* (1), eaav1851.

(8) Sholl, D. S.; Lively, R. P. Seven Chemical Separations to Change the World. *Nature* **2016**, *532* (7600), 435−437.

(9) Baker, R. W. Future Directions of Membrane Gas Separation Technology. *Ind. Eng. Chem. Res.* **2002**, *41* (6), 1393−1411.

(10) Wijmans, J.; Baker, R. The Solution-Diffusion Model: A Review. *J. Membr. Sci.* **1995**, *107* (1), 1−21.

(11) Yuan, Z.; Govind Rajan, A.; Misra, R. P.; Drahushuk, L. W.; Agrawal, K. V.; Strano, M. S.; Blankschtein, D. Mechanism and Prediction of Gas Permeation through Sub-Nanometer Graphene Pores: Comparison of Theory and Simulation. *ACS Nano* **2017**, *11* (8), 7974−7987.

(12) Koenig, S. P.; Wang, L.; Pellegrino, J.; Bunch, J. S. Selective Molecular Sieving through Porous Graphene. *Nat. Nanotechnol.* **2012**, *7* (11), 728−732.

(13) Huang, S.; Dakhchoune, M.; Luo, W.; Oveisi, E.; He, G.; Rezaei, M.; Zhao, J.; Alexander, D. T. L.; Züttel, A.; Strano, M. S.; Agrawal, K. V. Single-Layer Graphene Membranes by Crack-Free Transfer for Gas Mixture Separation. *Nat. Commun.* **2018**, *9* (1), 2632.

(14) Rajan, A. G.; Silmore, K. S.; Swett, J.; Robertson, A. W.; Warner, J. H.; Blankschtein, D.; Strano, M. S. Addressing the Isomer Cataloguing Problem for Nanopores in Two-Dimensional Materials. *Nat. Mater.* **2019**, *18* (2), 129−135.

(15) Yuan, Z.; Benck, J. D.; Eatmon, Y.; Blankschtein, D.; Strano, M. S. Stable, Temperature-Dependent Gas Mixture Permeation and Separation through Suspended Nanoporous Single-Layer Graphene Membranes. *Nano Lett.* **2018**, *18* (8), 5057−5069.

(16) Khan, M. H.; Moradi, M.; Dakhchoune, M.; Rezaei, M.; Huang, S.; Zhao, J.; Agrawal, K. V. Hydrogen Sieving from Intrinsic Defects of Benzene-Derived Single-Layer Graphene. *Carbon* **2019**, *153*, 458−466.

(17) Dutta, S.; Vahdat, M. T.; Rezaei, M.; Agrawal, K. V. Crystallization of Gas-Selective Nanoporous Graphene by Competitive Etching and Growth: A Modeling Study. *Sci. Rep.* **2019**, *9* (1), 5202.

(18) O'Hern, S. C.; Boutilier, M. S. H.; Idrobo, J.-C.; Song, Y.; Kong, J.; Laoui, T.; Atieh, M.; Karnik, R. Selective Ionic Transport through Tunable Subnanometer Pores in Single-Layer Graphene Membranes. *Nano Lett.* **2014**, *14* (3), 1234−1241.

(19) Boutilier, M. S. H.; Jang, D.; Idrobo, J.-C.; Kidambi, P. R.; Hadjiconstantinou, N. G.; Karnik, R. Molecular Sieving across Centimeter-Scale Single-Layer Nanoporous Graphene Membranes. *ACS Nano* **2017**, *11* (6), 5726−5736.

(20) He, G.; Huang, S.; Villalobos, L. F.; Zhao, J.; Mensi, M.; Oveisi, E.; Rezaei, M.; Agrawal, K. V. High-Permeance Polymer-Functionalized Single-Layer Graphene Membranes that Surpass the Post-combustion Carbon Capture Target. *Energy Environ. Sci.* **2019**, *12* (11), 3305−3312.

(21) O'Hern, S. C.; Jang, D.; Bose, S.; Idrobo, J.-C.; Song, Y.; Laoui, T.; Kong, J.; Karnik, R. Nanofiltration across Defect-Sealed Nanoporous Monolayer Graphene. *Nano Lett.* **2015**, *15* (5), 3254−3260.

(22) Baker, R. W.; Lokhandwala, K. Natural Gas Processing with Membranes: An Overview. *Ind. Eng. Chem. Res.* **2008**, *47* (7), 2109−2121.

(23) Bernardo, P.; Drioli, E.; Golemme, G. Membrane Gas Separation: A Review/State of the Art. *Ind. Eng. Chem. Res.* **2009**, *48* (10), 4638−4663.

(24) Gillespie, D. T. A General Method for Numerically Simulating the Stochastic Time Evolution of Coupled Chemical Reactions. *J. Comput. Phys.* **1976**, *22* (4), 403−434.

(25) Gastwirth, J. L. The Estimation of the Lorenz Curve and Gini Index. *Rev. Econ. Stat.* **1972**, *54* (3), 306.

(26) He, G.; Huang, S.; Villalobos, L. F.; Vahdat, M. T.; Guiver, M. D.; Zhao, J.; Lee, W.-C.; Mensi, M.; Agrawal, K. V. Synergistic CO_2-Sieving from Polymer with Intrinsic Microporosity Masking Nanoporous Single-Layer Graphene. *Adv. Funct. Mater.* **2020**, *30*, 2003979.

(27) Rezaei, M.; Li, S.; Huang, S.; Agrawal, K. V. Hydrogen-Sieving Single-Layer Graphene Membranes Obtained by Crystallographic and Morphological Optimization of Catalytic Copper Foil. *J. Membr. Sci.* **2020**, *612*, 118406.

(28) Bao, W.; Miao, F.; Chen, Z.; Zhang, H.; Jang, W.; Dames, C.; Lau, C. N. Controlled Ripple Texturing of Suspended Graphene and Ultrathin Graphite Membranes. *Nat. Nanotechnol.* **2009**, *4* (9), 562−566.

(29) Li, Z.; Wang, Y.; Kozbial, A.; Shenoy, G.; Zhou, F.; McGinley, R.; Ireland, P.; Morganstein, B.; Kunkel, A.; Surwade, S. P.; Li, L.; Liu, H. Effect of Airborne Contaminants on the Wettability of Supported Graphene and Graphite. *Nat. Mater.* **2013**, *12* (10), 925−931.

(30) Kozbial, A.; Zhou, F.; Li, Z.; Liu, H.; Li, L. Are Graphitic Surfaces Hydrophobic? *Acc. Chem. Res.* **2016**, *49* (12), 2765−2773.

(31) Robertson, A. W.; Lee, G.-D.; He, K.; Gong, C.; Chen, Q.; Yoon, E.; Kirkland, A. I.; Warner, J. H. Atomic Structure of Graphene Subnanometer Pores. *ACS Nano* **2015**, *9* (12), 11599−11607.

(32) Tanaka, H.; Kanoh, H.; Yudasaka, M.; Iijima, S.; Kaneko, K. Quantum Effects on Hydrogen Isotope Adsorption on Single-Wall Carbon Nanohorns. *J. Am. Chem. Soc.* **2005**, *127* (20), 7511−7516.

(33) Potoff, J. J.; Siepmann, J. I. Vapor−Liquid Equilibria of Mixtures Containing Alkanes, Carbon Dioxide, and Nitrogen. *AIChE J.* **2001**, *47* (7), 1676−1682.

(34) Jorgensen, W. L.; Maxwell, D. S.; Tirado-Rives, J. Development and Testing of the OPLS All-Atom Force Field on Conformational Energetics and Properties of Organic Liquids. *J. Am. Chem. Soc.* **1996**, *118* (45), 11225−11236.

(35) Cheng, A.; Steele, W. A. Computer Simulation of Ammonia on Graphite. I. Low Temperature Structure of Monolayer and Bilayer Films. *J. Chem. Phys.* **1990**, *92* (6), 3858−3866.

(36) Callen, H. B. *Thermodynamics and an Introduction to Thermostatistics*, 2nd ed.; John Wiley & Sons: New York, 1987.

(37) Towns, J.; Cockerill, T.; Dahan, M.; Foster, I.; Gaither, K.; Grimshaw, A.; Hazlewood, V.; Lathrop, S.; Lifka, D.; Peterson, G. D.;

https://dx.doi.org/10.1021/acsnano.0c09420
ACS Nano 2021, 15, 1727−1740

Roskies, R.; Scott, J. R.; Wilkins-Diehr, N. XSEDE: Accelerating Scientific Discovery. *Comput. Sci. Eng.* **2014**, *16* (5), 62−74.

https://dx.doi.org/10.1021/acsnano.0c09420
ACS Nano 2021, 15, 1727−1740